We are IntechOpen,
the world's leading publisher of
Open Access books
Built by scientists, for scientists

6,900
Open access books available

185,000
International authors and editors

200M
Downloads

154
Countries delivered to

Our authors are among the

TOP 1%
most cited scientists

12.2%
Contributors from top 500 universities

CLARIVATE ANALYTICS
BOOK CITATION INDEX
INDEXED

WEB OF SCIENCE™

Selection of our books indexed in the Book Citation Index
in Web of Science™ Core Collection (BKCI)

Interested in publishing with us?
Contact book.department@intechopen.com

Capillary Bridges — A Tool for Three-Phase Contact Investigation

Boryan P. Radoev, Plamen V. Petkov and
Ivan T. Ivanov

Additional information is available at the end of the chapter

Abstract

Subject of investigation are capillary bridges (CB) between two parallel solid plates normally oriented to the gravity field. Presented are results of study of CB with negligible gravity effects and CB undergoing observable gravitational deformations. Among the discussed problems some new aspects of the CB behavior are formulated. One of them is the so-called stretching thickness limit, i.e. the maximal thickness above which a CB of given volume and contact angles cannot exist. It is shown that the stretching thickness limit of a concave CB substantially differs from that of a convex one. Analysis of the forces acting on CB plates is presented. It clearly demonstrates that the gravity part of the forces, relative to the part of capillary forces, increases with stretching. Most of the observed effects are interpreted on the basis of the two CB radii of curvature analysis, thus avoiding the ponderous procedures of obtaining (integrating) the CB generatrix profile. The success of this approach lies in its combination with image analysis of CB profile. Discussed are the contact angle hysteresis effects at CB stretching and pressing.

Keywords: capillary bridge, image analysis, contact angle hysteresis

1. Introduction

As every classical subject, the capillary bridge (CB) has its centuries-old history and continuous reincarnation in the science and praxis. A characteristic feature of the classical subject is the

richness of problems they produce. CB related human activity goes back to the ancient times [1, 2]. Nowadays CB provide well-known effects in atomic force microscopy [3, 4] and lithography [5-8]. CB also play important role in soil-water interactions [9-11].

The scientific interest of CB originates from the mathematical problem of construction of figures of minimal area, defined by the French astronomer and mathematician C. Delaunay [12]. He found a new class of axially symmetric surfaces of constant mean curvature. Much later Kenmotsu [13] solved the complex nonlinear equations, describing this class of surfaces. However, the solution that he had proposed has little practical importance because the representation there has no geometrical interpretation.

An important step in the analysis of minimal surfaces is the understanding of the role of their curvatures. Today it is well known that a surface of minimal area has a constant mean curvature and vice versa [12], but the formulation and the proof of this theorem have their long story. It begins with the remarkable figure proposed by Euler [14], named later catenoid [15]. In the mathematical studies, the catenoid is defined as a figure of revolution with zero mean curvature but for the rest of the natural sciences it is popular as an object, formed by a soap film stretched between two parallel rings. The fundamental question here is what physical feature of soap films determines their minimal areas. The answer of this question is the surface tension, nowadays given at school, but it took almost a whole (18th) century for that answer. Many scientists have contributed to the elucidation of the problem, two of them: Pierre Simon Laplace (1749-1827) and Thomas Young (1773-1829) [16] are of the greatest merit. To these two scientists and especially to one of them, Laplace, we owe the introduction of the notion of capillary tension, which opened the way of modern investigation of capillary phenomena. Moreover, Laplace has practically formulated the currently used condition for mechanical equilibrium between two fluids divided by a capillary surface, $p_\sigma = \Delta p$. Here $p_\sigma = \sigma(1/R_1 + 1/R_2)$ is the capillary pressure with surface tension σ, radii of curvature are $R_{1,2}$ and the pressure difference between the adjacent bulk phases is Δp (isotropic fluids). The sum $(1/R_1 + 1/R_2)$ is twice the so-called mean curvature. Note that the cited above Laplace formula has its gener-alized form for anisotropic fluids (e.g. liquid crystals) [17]. Among all parameters of the Laplace formula, most interesting are the radii of the curvature $R_{1,2}$. They are the tool for investigation and analysis of the variety of capillary shapes. The analytical interpretation of the mean curvature is based on the differential geometry but its combination with the direct geometrical meaning of the radii proves to be very fruitful. For surfaces of revolution, this geometrical meaning becomes very transparent. Along with that, the analytical expressions of their radii $R_{1,2}$ take on specific form facilitating their further analysis. Expressive examples in this respect with wide application in the academic and applied research are CBs [18, 19]. As a geometric subject, surfaces of revolution are formed by rotation of a curve (called generatrix) around a given axis. From here it follows that each of their cross-sections with a plane perpendicular to the axis of revolution is a circle. In the reality, two solid plates play the role of the parallel planes. This simple geometric figure imposes strict requirements regarding the solid CB plates. More about the solid plates, used in our experiments, can be found in Section 4. They must be: (1) macroscopically smooth (without roughness) and (2) homogeneous (with constant surface energy). An axial symmetrical CB can be formed between many combinations of solid surfaces

(e.g. between two co-axial spheres, cone and plane, etc.) but the prevailing part of the re-searches are focused exclusively on bridges between parallel flat plates. As we will discuss the role of gravity, the axis of revolution must be parallel to the gravity field. A general survey of a CB in a gravitational field at arbitrary orientation and inertia fields can be found in [20]. The smoothness and homogeneity of solid surfaces are genetically related to the so-called three-phase contact (TPC) angle hysteresis. In more details, this topic will be discussed in Sections 3-4. Here we will make only a short remark. A widely spread opinion is that hysteresis is a result of surface roughness and heterogeneity, i.e. on macroscopic smooth and homogeneous surfaces hysteresis should not be observed [21]. As an illustration of this opinion usually the undisputed lack of hysteresis of oil droplet on water (immiscible liquids) is considered. Liquid surfaces are naturally smooth and homogeneous but in the same time they (actually the Newtonian liquids) have a very specific rheological property, they do not bear shear stress at equilibrium in contrast to the solids. This difference is crucial for the dynamics of the systems. A droplet on liquid will be set in motion by any nonzero (tangential to the three phase contact) force, while a droplet on solid could stay at rest, as the solid substrate can react to the opposed force by static shear stress [22, 23]. Here it is important to remind the experimentally proven nonslip model in the fluid dynamics. The nonslip model is a special case of the more general concept of continuum (e.g. [24]). According to this model, within fluids as well as their boundaries, the velocity field is continuous. This continuity model is based on the intermo-lecular (van der Waals) forces' existence. More precisely, on the presumption that the part of an external force per intermolecular region is negligible with respect to the van der Waals forces [25]. Hydrodynamic problems connected with the TPC line motion have made some authors to give up the nonslip presumption [26, 27, 28, 29]. Most popular are two alternatives: the hypothesis of local slippage in the TPC vicinity [30] and the model based on Eyring theory [31, 32]. A weakness of these approaches is neglecting of the so-called surface forces [33, 34]. These forces result directly from intermolecular forces and become significant in thin gaps (thickness < 10 nm) between two surfaces, i.e. just in the TPC zones, where the hydrodynamic singularities arise. The interested reader can find more about the role of surface forces for the wetting in [35]. In our experiments we have observed hysteresis in a wide range: from practically pinned contacts (strong hysteresis) to contacts with nearly constant contact angles and we have tried to interpret it in the framework of nonslip convention.

Most of the problems discussed in this chapter are well known. They concern not only CB between two flat parallel solid surfaces but also other specific CB types (Appendix C). Some nontrivial results obtained here are related to the study of the CB upper stretching limit. Usually this problem is discussed from the stability viewpoint but it should be treated as a critical point. The critical point is defined as a boundary equilibrium state, i.e. a system cannot exist outside the critical point. Of course, this state could be unachievable, if it is preceded by instable states. As known from the theory [36], the stability concerns the reaction of the system at perturbation of a given equilibrium state. If the reaction is a tendency to return the system in the equilibrium, this state is stable, otherwise the state is unstable. A typical example, illustrating the difference between critical and instable states, is a CB with cylindrical form, i.e. a CB with a 90° contact angle. From an equilibrium viewpoint, a cylindrical CB can be stretched without limitations, i.e. $H_{cr} \to \infty$ (H – CB thickness). On the other hand, cylindrical

CB have stability limit $H_{stab}=\pi R$ (R – cylinder radius), the so-called Rayleigh instability, above which a cylindrical CB becomes unstable [37, 38]. A more detailed analysis of CB critical points is provided in Section 2. Actually, the stability problems are beyond the scope of this study.

2. Definition of the subject

Subject of investigation, as already mentioned, is a capillary bridge between two parallel solid plates, normally oriented to the gravity field (Figure 1). Only axisymmetric bridges are considered, i.e. CBs with circle three phase contacts. Although the analysis is performed for equal contact angles on the upper/lower plate ($\theta_+=\theta_-;R_+=R_-$), it is shown that most of the theoretical results are also applicable for different contact angles/radii – Section 2.
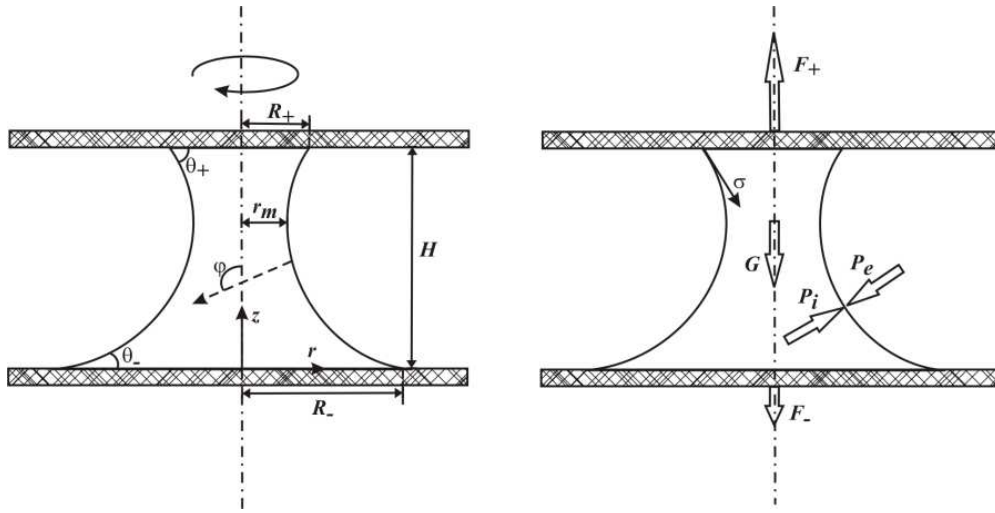

Figure 1. *Sketch of capillary bridge in gravity field. Left*: CB geometric parameters; *Right*: CB dynamic parameters, G – CB weight, $F_\pm$ – external forces, $G + F_+ + F_- = 0$ (about the notations see in the glossary and text)

The processes of evaporation, condensation and the related potential temperature effects [39, 40, 41] won't be discussed. Water bridges have shown observable evaporation, which was neglected, because the evaporation rates were low enough, thus ensuring quasi-static states of the CB, Section 4. Moreover, the scaled forms of the theoretical results are invariant to the bridge volume, Eq. (8). Concerning the RTIL bridges, they are practically non-volatile.

As known, the mechanical equilibrium of a capillary system obeys the pressure balance, $p_\sigma=\Delta p$, where p_σ is the capillary pressure and Δp is the pressure difference of both sides of the capillary surface. Because of the axial symmetry, $p_\sigma=\sigma r^{-1}d(r\sin\varphi/dr)$, where r and φ are current coordinates. In this symmetry, the separate curvatures ($1/R_{1,2}$) are defined as follows: $1/R_1=\sin\varphi/r$ (the so-called azimuthal curvature); $1/R_2=d\sin\varphi/dr$ (meridional curvature). The angle φ is defined between the normal vector at a given point of the generatrix and the vertical axis z, Figure 1 left. In this study the CB pressure difference is defined as $\Delta p = p_i - p_e$ where $p_{i/e}$

are internal/external pressures, Figure 1 right. The external pressure is practically constant (p_e = $const$), while the inside pressure varies with height (hydrostatic pressure), $p_i = p_0 - \rho g z$. The precise expression of the gravitational term is $\Delta \rho g z$, where $\Delta \rho = \rho_{liquid} - \rho_{air} \approx \rho_{liquid} \equiv \rho$ (the air density is negligible compared to liquid density). We use traditional notations as: ρ − density and g − gravity of earth. The inside pressure p_0 at level $z=0$ deserves special attention. In its turn, the zero vertical position is a question of choice, Sections 2 and 3. Inserting all briefly explained quantities in the pressure balance, one obtains [18, 42]:

$$\sigma \frac{1}{r} \frac{d}{dr}(r \sin \varphi) = \Delta p_0 - \rho g z, \tag{1}$$

with $\Delta p_0 = p_0 - p_e$. The main mathematical complication in Eq. (1) comes from the non-linear relation between $\sin \varphi$ and the generatrix equation $z(r)$, $\sin \varphi = (dz/dr)/\sqrt{1 + (dz/dr)^2}$. At the same time, the use of $\sin \varphi$ as variable show advantages which are repeatedly demonstrated in the present study.

A preparatory and very important step for the successful solution and analysis of any differential equation is its scaling. Particularly the scaled form of Eq. (1) reads:

$$\frac{1}{x} \frac{d}{dx}(x \sin \varphi) = P_0 - Bo\, y, \tag{2}$$

where $x \equiv r/L_r$; $y \equiv z/L_z$; $P_0 \equiv (\Delta p_0)L_r/\sigma$; $Bo \equiv \rho g L_r L_z/\sigma$. Generally scaling lengths (here, L_r, L_z) are derived from the dimensions of the system and are chosen so that the order of the scaled (dimensionless) variable is of the order of unity. So, for instance, in the case of a CB, the vertical scaling length obviously is the bridge height, i.e. $L_z = H$. To know more about the concrete scaling procedures, see in Sections 2 and 3. The dimensionless parameter Bo, known as Bond number [43, 20] is decisive for the role of gravity in the capillary systems. Most often the criterion for neglecting the effects of gravity is written as $Bo \ll 1$ but as it can be seen from Eq.(2), the correct condition is $Bo \ll P_0$. More generally, the scaled form Eq. (2) is the stepping stone for solving the generatrix equation $z(r)$ in Bo powers series, $z(x) = z_0(x) + z_1(x)Bo + \dots$ for arbitrary values of $Bo < P_0$. Another often noticed misleading usage of the Bond number concerns the scaling lengths L_k. Usually they are reduced to only one length, which in the case of a CB is most often the contact radius, i.e. $Bo \equiv \rho g R^2/\sigma$ [44, 45]. Eq. (1) also allows an interesting comparative analysis of the two curvatures $1/R_{1,2}$, Section 3. As an illustration of such analysis, let's consider the curvatures in the CB waist/haunch point. The azimuthal curvature reduces to $1/r_m$ (r_m, waist/haunch radius, Figure 1), while the meridional curvature preserves its form ($d \sin \varphi/dr$). Now let us imagine a flattening of CB at constant contact angles. It is obvious that the azimuthal curvature will diminish (r_m grows), while the meridional curvature $d \sin \varphi/dr$ increases. Moreover, in Section 2 it is shown that $d \sin \varphi/dr \to \infty$ at $H/R \to 0$, Appendix A. In conclusion, it follows that the balance, Eq. (1) allows different type of approximations, e.g. a weightless CB ($Bo=0$, Section 2), a heavy CB ($Bo \neq 0$, Section 3); 2D/3D bridges (Section 3).

3. Capillary bridge in the absence of gravity

This section is devoted to a CB for which the role of gravity is negligible compared with the capillary pressure. According to Eq. (2), the pressure balance in this case takes the form [42]:

$$\frac{1}{x}\frac{d}{dx}(x\sin\varphi) = P_0, \tag{3}$$

with a criterion for its validity $Bo \ll P_0$. The CB Bond number is expressed as $Bo = \rho g L_r H / \sigma$, where H is the bridge thickness and L_r is the radial scaling length (Section 1). As shown at Figure 1, there are two variants for choice of L_r: the contact radius R or the haunch/neck radius r_m and below it will be shown that r_m is the preferable one. Before that, let's briefly consider the factors determining the Bo magnitude. The parameters in Bo can be grouped in two parts, a physical part ($\varrho g/\sigma$) and a geometric ($L_r H$) one. The physical complex ($\varrho g/\sigma$), often related to the so-called capillary length, $L_\sigma \equiv \sqrt{\sigma/\rho g}$ is a constant for a given liquid. For instance the capillary length of water is of the order of millimeters ($\sigma \approx 70$ mN/m; $\varrho \approx 10^3$ Kg/m^3; $g \approx 10$ m/s^2), $L_\sigma \approx 1\,mm$. The variable parameters in our experiments are the geometric lengths, L_r and H. They are not independent but coupled, roughly speaking, as $L_r^2 \sim 1/H$ (constant volume, $V \sim L_r^2 H$). From here it follows that $Bo \sim \sqrt{H}$, i.e. at CB flattening (thinning) the role of gravity decreases.

The first integral of the pressure balance Eq. (3) causes no difficulty and using the boundary condition $\varphi(r = r_m) = 90°$, one obtains,

$$x\sin\varphi = C(x^2 - 1) + 1, \tag{4}$$

Note that here, in accordance with the above-mentioned boundary condition, the scaling length is the waist/haunch radius r_m and the dimensionless parameters are $x \equiv r/r_m$ and $C \equiv \Delta p_0 r_m/2\sigma$ respectively. The notation C of the scaled capillary pressure instead of P_0 is to emphasize the difference between Δp_0 of heavy and weightless CB. In presence of gravity (heavy CB), Δp_0 is referred to the CB bottom while in absence of gravity (weightless CB) Δp_0 is a global characteristic. The scaled capillary pressure C plays central role in the entire CB analysis below. Very indicative, for instance is its relation with the TPC radii R and angles θ. Applying Eq. (4) to the upper/lower contact ($x = X_\pm$) one obtains:

$$C = \frac{X_\pm \sin\theta_\pm - 1}{X_\pm^2 - 1}, \tag{5}$$

where, $X_\pm \equiv R_\pm/r_m$. Actually Eq. (4) holds for any cross section of CB with a plane (normal oriented to the axis of symmetry) relating a (X, θ) couple at the respective level y. This general consideration allows us for the sake of simplicity to use Eq. (5) in form $C(X, \theta)$, Figure 2. Relation

(5) clearly shows the algebraic character of C, i.e. the algebraic character of the capillary pressure P_γ. It can be positive, zero or negative. At convex generatrix ($X<1$), in the entire interval of angles ($\pi/2<\theta\leq\pi$), the capillary pressure is positive ($C>0$). The intercept points of the dashed line $C=1$ with the isogons (Figure 2) correspond to spherical CB forms, i.e. circular arc generatrix curves. As seen from Eq. (5), the spherical CB parameters satisfy the condition $X=\sin\theta$. An exception is the point $C(X=0)=1$, which is a peculiar end point of all convex CB ($\theta>\pi/2$) isogons. As it will be discussed below in this section, approaching (by stretching) $X \to 0$, i.e. at $r_m \to 0$, the convex isogon generatrix $y(x)$ pass through inflexion point ($d^2y/dx^2=0$, Eq. (10)). Another noteworthy region of C vs. X diagrams is the line $X=1$. It is the asymptote of concave/convex isogons ($C \to \pm\infty$) and the discontinuity point $\{C=1/2, X=1\}$ lies also on it. The regions $C \to \pm\infty$ concern the so-called thin CB, Appendix A, while the point $\{C=1/2, X=1\}$ acquires cylindrical shape (contact angle $\theta=\pi/2$). Cylindrical CB is an attractive capillary subject because of its simple form, making the stability problems very transparent [46].
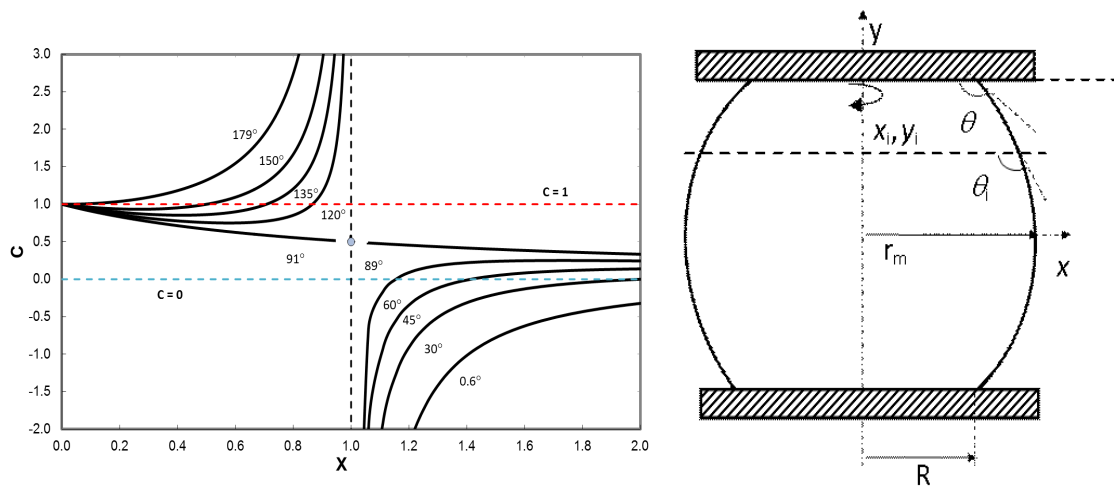

Figure 2. *Left* – Capillary pressure, *C vs X*, calculated from Eq. (5); *Right* – arbitrary cross section illustrating a convex CB with constant *C* but different contact angles θ, θ$_i$.

Zero capillary pressure ($C=0$) defining a catenoid state is one of the most popular capillary figures. We have already mentioned about it in the Introduction and here will add only the condition for its realization, $X\sin\theta=1$, Eq. (5), illustrated by the cross point of the dashed horizontal line $C=0$ with the isogons $\theta<\pi/2$ (Figure 2 left). The region $X>1$ corresponds to stretching of concave CB. Below in the text it will be shown that there are critical values of (X, θ) above which concave CB do not exist.

The external forces, $F_\pm$ supporting a CB are another very important characteristic, which can be obtained via elementary tools. At negligible gravity, $F_\pm$ are equal in absolute value but oppositely directed, $\vec{F}_+ + \vec{F}_- = 0$ (Figure 1). As derived in Appendix B, due to the gravity, the relation between $F_\pm$ gets more complicated. In contrast to liquid|gas surface where the mechanical equilibrium is described by a local balance, Eq. (3), the forced balance on solid|liquid; solid|gas can be derived only globally. Due to the force acting on the entire solid area and on the TPC contact contour, one obtains [42].

$$F_{\pm} = \pm(2\pi R_{\pm}\sigma \sin\theta_{\pm} - \pi R_{\pm}^{2}\Delta p_{0}) \tag{6}$$

Because of the trivial symmetry, we will further analyse only the balance on the upper plate, thus omitting the subscript (+). The term $2\pi R\sigma\sin\theta$ is the normal (toward the contact plane) component of the TPC force and the term $\pi R^{2}\Delta p_{0}$ is the capillary pressure force. Upon expressing Δp_{0} through C from Eq. (5), we finally obtain F:

$$F = 2\pi\sigma R\frac{X - \sin\theta}{X^{2} - 1}. \tag{7}$$

Like the capillary pressure, Eq. (5), the force F can alter its sign or become zero. At concave CB, since $X \geq 1$, F is positive for all angles in the interval $0 \leq \theta \leq \pi/2$ and acts as a stretching force. At convex CB ($X<1$) the external force F is positive at $(\sin\theta - X)>0$, zero ($F=0$) in the point $\sin\theta = X$, (spherical CB, Eq. (4) at $C=1$) and negative pressing force ($F<0$) at $X>\sin\theta$.

The complete analysis of CB behavior requires integration of Eq. (4). In essence, this integration yields the generatrix equation $y(x)$ which in our notations can be presented as [47]:

$$y(x,C) = \frac{RI_{0}(x,C)}{X}, \text{ with } I_{0}(x,C) = \pm\int_{1}^{x}\frac{1+C(\xi^{2}-1)}{\sqrt{\xi^{2}-\left[1+C(\xi^{2}-1)\right]^{2}}}d\xi, \tag{8}$$

The integral $I_{0}(x,C)$ describes the upper part of the generatix curve, i.e. at $0 \leq y \leq H/2r_{m}$ (above the neck, Figure 1 left). Note that here, for the sake of convenience, the co-ordinate system is established on the CB neck/haunch with (scaled) radial coordinate defined in the interval $1 \leq x \leq X$ ($=R/r_{m}$) for concave CB and $X \leq x \leq 1$ for convex CB respectively. The sign '$\pm$' accounts whether the CB is concave (positive sign, $X >1$, $0 \leq \theta < \pi/2$), or convex (negative sign, $X <1$, $\pi/2 < \theta \leq \pi$). Further the signs of I_{0} will be omitted, given the correct sign in every particular situation. Traditionally I_{0} is presented by (Legendre's) elliptic integrals first and second kind F, E (e.g. [18]), but for its evaluation we apply another calculation scheme (see further).

As seen I_{0} is integrable, but singular (in the lower limit $\xi=1$), which gives rise to significant instability of the numerical results. We have settled the issue by dividing the integrals into singular and regular parts. The singular part allows direct integration, while the regular part is estimated numerically and as a result, for $x=X$ one obtains:

$$I_{0}(X,C) = \frac{\pi}{4C} - \frac{1}{2C}\arcsin\left[\frac{(1-2C)-2C^{2}(X^{2}-1)}{(1-2C)}\right] - \int_{1}^{x}\sqrt{\frac{\xi-\left[C(\xi^{2}-1)+1\right]}{\xi+\left[C(\xi^{2}-1)+1\right]}}d\xi, \tag{9}$$

In practice, the evaluation of I_{0}, according to Eq. (9), is performed by assigning a series of values of X at a fixed contact angle θ. The computation procedure is split into two subintervals $X >1$, $0 \leq \theta < \pi/2$ (concave CB) and $X <1$, $\pi/2 < \theta \leq \pi$ (convex CB). We have used for X step of $\Delta X = 0.05$; the angles subject to computation were: 15°, 30°, 45°, 60°, 89°; 91°, 100°, 120°, 179° (Figure 3, Figure 4).

Most of the evaluations here concern experimentally measured quantities. As all measure‐
ments are optical, it is preferable the experimental data to be presented in a form invariant
with respect to the optical magnification. An appropriate presentation is H/R vs X, very
convenient for interpretation by the theoretical relation following from Eq. (8) at
$x = X$, $H / R = 2I_0(X, C) / X$. Formally the ratio (H/R) is function of X and C, but the parameter
C is function of X and contact angles $\theta_\pm$ Eq. (5) which transforms (H/R) equivalently in a
function of X and θ, $H / R = f(X, \theta)$. It's important to note that the additional condition of

constant volume $V = 2\pi r_m^3 \int_1^X \xi^2 dI_0(\xi, C) = const$ is necessary for the determination of the radii R

or r_m separately [47].

Figure 3 and Figure 4 present series of curves (H / R) vs. X^{-1}, respectively vs. X calculated via
Eqs. (8)-(9) for a set of contact angles. The coordinate X^{-1} in Figure 3 has been favored for its
more compact presentation $(0 \leq X^{-1} \leq 1)$, compared to X $(1 \leq X < \infty)$. The limit $X \to 1$ named here
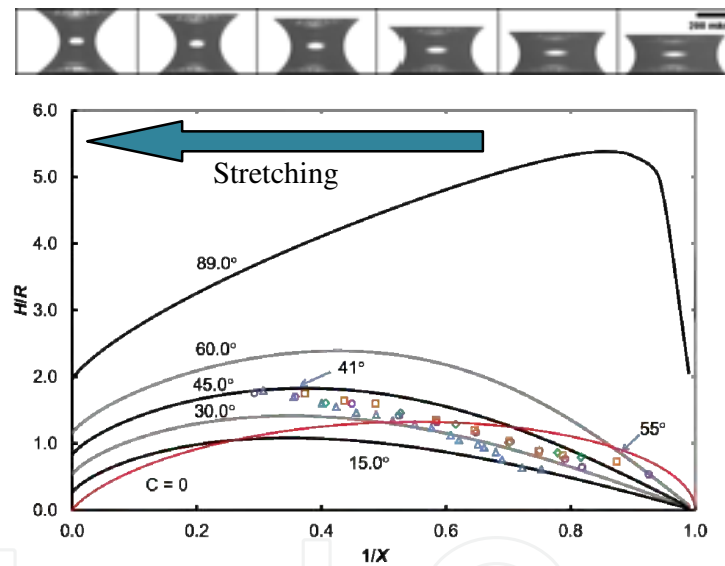thin CB will be discussed in more details in Appendix A.

Figure 3. Data from several experiments (triangles, hollow circles and squares) of stretching concave CB. The meas‐
ured contact angles indicated apparent hysteresis. The photo series above illustrate the real CB shape deformation at
stretching.

The most substantial difference between the graphics of Figure 3 and Figure 4 is the presence
of maximum only in one of them. On the one hand, $(H/R)_{max}$ is a critical value, i.e. a (concave)
CB can't be stretched more than this degree. On the other hand, the existence of extremum
puts the question which of the two $1/X_m$ at a given (H/R) is the real one? This well-known
problem in the literature is solved via thermodynamic considerations. The right branch of an
concave isogone $[(1/X_m) < (1/X) < 1]$ is the so called thermodynamic stable branch, while the left
branch is thermodynamic unstable one. These two branches define equilibrium states but with
different liquid|gas area. The CBs on the left branch are with bigger area compared with the
CBs on the right branch and this is maybe the most transparent elucidation of the question [46].

Now the question is why the convex CB ($\theta > \pi/2$) show no extremum? A short (and correct) but not so transparent answer is because the two curvatures of convex CB have same sign in contrast to concave CB, where the curvatures have opposite signs. The upper limit of stretching of convex CB is at $X=0$, i.e. at $R=0$. It is the same limit as in the case of $C(X=0)=1$ (Figure 2), where all convex isogons end at one point. It is interesting to note that in the state $R=0$ the parameter C acquires the value coinciding with the value of C for a sphere ($C=1$). The problem here is that the complete (closed) sphere is only congruent with a contact angle $\theta = 180°$, while for all other angles the asymptote $R \rightarrow 0$ calls for additional analysis. The solution of the problem is associated with the appearance of an inflexion point x_i in the generatrix, i.e. with the appearance of a root in $(d^2y/dx^2)_{x_i}=0$. From Eq. (8) one obtains:

$$x_i^2 = \frac{1-C}{C} = X\frac{\sin\theta - X}{1 - X\sin\theta}, \qquad (10)$$

It ensues from Eq. (10) that the inflexion emerges in the range $0 < X < \sin\theta$, i.e. beyond the "sphere" state $X = \sin\theta$. More details about the inflexion point can be found in [42, 47]. Figure 5 illustrates the appearance of inflexion point for two angles (95°, 120°) at stretching. It is clearly seen that at $\theta = 180°$ any signs of inflexion are absent.

On Figure 3 and Figure 4 experimentally measured points of CB stretching are drawn. The direct measurements of contact angles show good coincidence with the theoretical isogons angle, which is a positive test of the method. The experimental data show also some interesting features of the TPC hysteresis. As seen, concave CB exhibits expressed hysteresis (contact angles θ change 10°-15°) while convex CB show now detective one (all experimental points lie close to $\theta \approx 100°$ isogone). Another noticeable difference in the TPC behavior between concave and convex CB is the reaction of the lower/upper contacts at stretching. Convex CBs show observable difference between the upper/lower contact radii ($R_\pm$) and angles ($\theta_\pm$), while the same parameters of concave CBs remain practically equal.
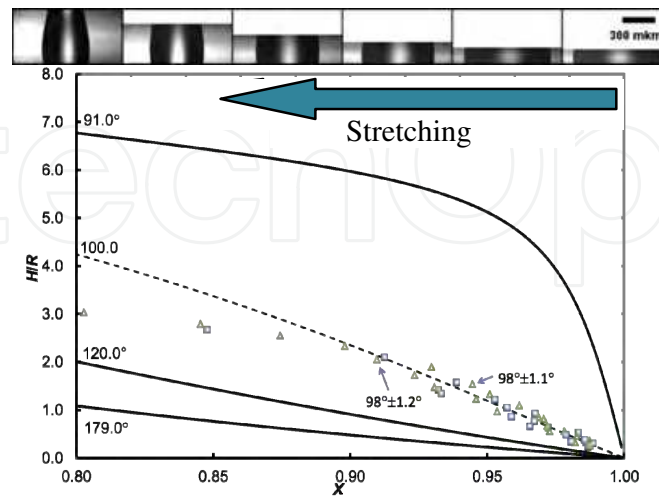

Figure 4. Data from stretching convex CB experiments (triangles and squares). The contact angle at weak stretching ($X=0.99 \div 0.91$) is practically constant. The deviation from the isogone at stronger stretching is due to gravity. The photo series above illustrate the real CB shape deformation at stretching.
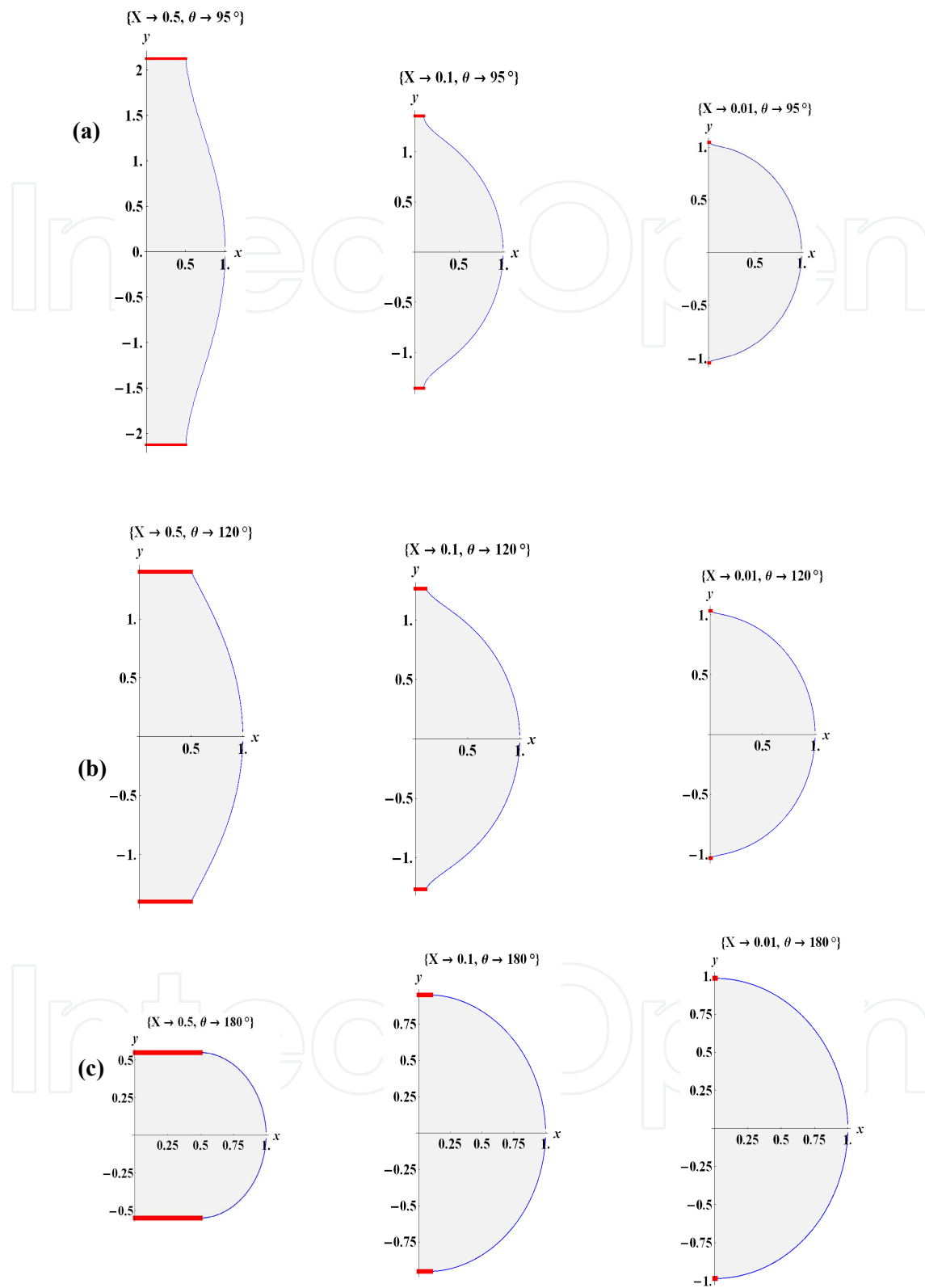
Figure 5. Capillary bridge profiles computed for three different states (X = 0.01, 0.1, 0.5) of three isogones in dimension-less coordinates $y = y(x)$: (a) $\theta = 95°$; (b) $\theta = 120°$; (c) $\theta = 180°$. The appearance of an inflexion is distinctly perceptible at increased stretching ($X = 0.1, 0.5$) at $\theta \neq 180°$.

The domain of rupture of the investigated convex CB turned to be at $X = 0.84 \div 0.80$, significantly earlier than the definition limit $X = 0$. The reason for the premature rupture could be the rise of *Rayleigh* instability [37], combined with the gravitational deformation. Yet, this phenomenon requires its own analysis.

4. Capillary bridge in a gravity field

In this section we will look into an aspect that is always present but often neglected. It is the role of gravity field on capillary forms. The work of Bashforth & Adams [48] from over a century ago is among the first reports exploring the effects of gravity on capillary shapes applying numerical methods for calculation of their shape. Latter many authors, e.g. [48, 49, 50, 51, 52, 20], proposed in the manner of Bashforth & Adams' work, new parameterization of the Laplace equation and thus defining the shape parameters of both bound and unbound axisymmetric menisci. Although these works have basically resolved the issue, there are still blank spots which need to be filled. We propose a slightly different variant of the classical approach, consisting of relatively simple instruments which allow us to obtain many interesting results, some of which are used for the interpretation of the experimental data.

A basis for the further analysis is the capillary gravitational balance in its dimensional Eq. (1) and scaled Eq. (2) forms. In contrast to CB, in the absence of gravity where the first integral of the pressure balance causes no difficulties, Eq.(4), the appearance of the gravitational term makes only its global integration transparent. In Appendix B one can find detailed derivation of all interesting relations, while here are given only the most substantial results. Among them are the external forces $F_{\pm}$ supporting CB in mechanical equilibrium (Figure 1 right). The emphasis *mechanical* is because the system could be thermodynamically non-equilibrium (e.g. to evaporate) which does not disturb the mechanical equilibrium.

As derived in Appendix B, Eq.(28), the upper/lower external forces $F_{\pm}$, get the form:

$$F_+ = \pi R_+ \frac{2\sigma r_m (R_+ - r_m \sin\theta_+) + R_+(G_+ / \pi - \rho g r_m^2 h_+)}{R_+^2 - r_m^2}$$

$$F_- = -\pi R_- \frac{2\sigma r_m (R_- - r_m \sin\theta_-) - R_-(G_- / \pi - \rho g r_m^2 h_-)}{R_-^2 - r_m^2},$$

(11)

The two parameters $R_{\pm}$, $\theta_{\pm}$ depend differently on gravity. In the case of identical substrates and ideal contacts (i.e. without hysteresis), the contact angles must be equal ($\theta_+ = \theta_- = \theta$) regardless of gravity, as far as they reflects situations of TPC governed by the van der Waals and electrostatic forces [33, 35]. Generally $\theta_+ \neq \theta_-$ as far TPC hysteresis is always present at solid surfaces. Compared to contact angles, contact radii $R_{\pm}$ are functions of gravity and differ one

from another ($R_+ \neq R_-$) even at equal angles θ. This can be proved easily by putting $\theta_+ = \theta_-$; $R_+ = R_-$ in Eq. (11) from where it follows $G=0$. From Eq. (11) follows that only F_- may nullify ($F_-=0$), while F_+ is non-zero, except at the trivial case when $R_+=0$. Note that in the case $R_+=0(R_-\neq0)$ we don't have bridge but a sessile droplet.

The situation ($F_-=0; F_+\neq0; R_+\neq0$) is equivalent to a pendant CB, similar to pendant droplet, where the whole weight is balanced by the external force at the upper plate, $F_+=G$. Of course for the sake of simplicity here the weight of CB plates is neglected.

As mentioned many times, the solution for heavy CB profile, $z(r)$ is a matter of profound numerical calculus, which actually is a combination of different approximations with semi-empirical numerical methods. Over the past decade, the development of this methodology has seemingly been completed. The research now is focused mainly on applications related to practical problems, [53, 54]. Below we demonstrate a known but not often used approach [55], marked by its geometrical transparency revealing some new insides of CB profiles.

To begin with, let's remind of the comparative analysis of the main curvatures $1/R_{1,2}$ made in Section 1.The radii of curvature $R_{1,2}$ depends quite differently on the CB dimensions, height H and contact radius R. On flattering the azimuthal radius $R_1=r/\sin\varphi$ increases while the meridional $R_2=dr/d\sin\varphi$ always decreases. This behavior derives directly from CB volume conservation condition. In addition, the meridional radius R_2 depends on the contact angle θ. So for instance, at $\theta=90°$ (cylindrical bridge), $R_2=0$ and the capillary pressure solely remains functional on R_1, ($p_\sigma=\sigma/R_1$). A detailed analysis of this and many other aspects can be found in Section 2. What is important here is the existence of CB heights interval, where $1/R_1<1/R_2$ so that the left hand side of Eq. (1) to be simplified as $\sigma d(\sin\phi)/dr = \Delta p_0 - \rho gz$. From geometric viewpoint, neglecting the azimuthal curvature reduces the problem from $3D$ to $2D$, and thus facilitating its analysis. The advantage comes from the trigonometric relation, $d\sin\varphi/dx = -d\cos\varphi/dz$ so that we can rewrite the equation of balance as

$$\sigma d(\cos\varphi)/dz = -\Delta p_0 + \rho gz, \qquad (12)$$

Now Eq. (12) can be integrated directly but before that let's look at the validity of this approximation from experimental viewpoint.

In Figure 6, experimental results about curvature ratio $(1/R_2)/(1/R_1)$ in the waist ($R_1=r_m$) of a concave CB as a function of its thickness ratio H/H_{cr} are given. The meridional curvature is notated as K and the thickness is scaled by the CB rupture thickness H_{cr}. The negative sign of the ordinate accentuates on the different curvatures' orientations (a concave CB), while for a convex CB the same ordinate would be positive. As seen from the diagram for a thickness up to $H/H_{cr}\leq0.6$, the meridional curvature is bigger (in absolute values) than the azimuthal curvature, i.e. in this range the $2D$ approximation holds. Series of experimental photos corresponding to the diagram data are shown above the diagram.
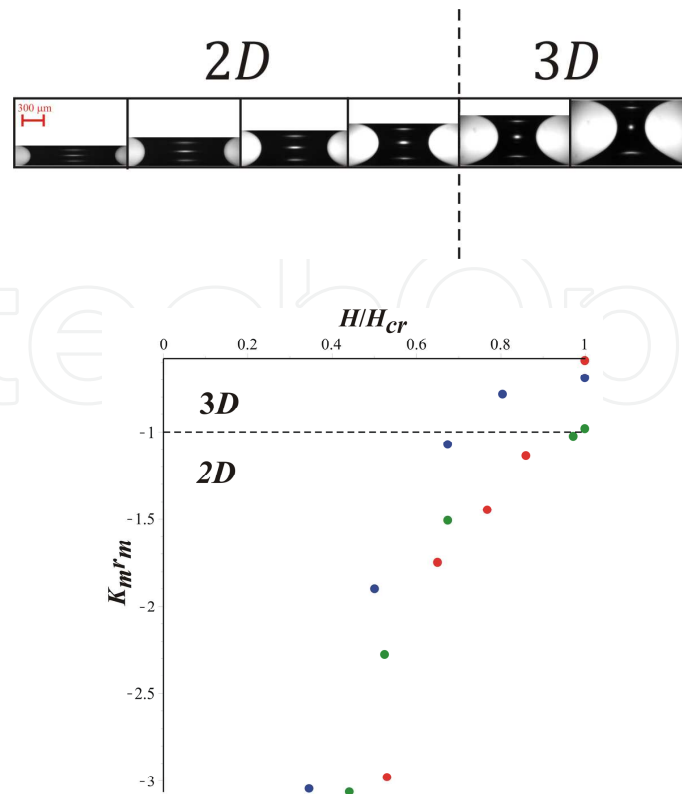
Figure 6. Experimental results for the curvature ratio ($K_m r_m$) vs. the thickness ratio H/Hcr; Hcr is the thickness of CB rupture; green – IL_4; blue – IL_5; red –IL_6; the transition $2D \rightarrow 3D$ is marked on the photo series.

The first integral of Eq. (12) in scaled version reads,

$$\cos \varphi = Bo y^2 - Cy + A, \tag{13}$$

with $Bo = \rho g H^2 / 2\sigma$; $C \equiv (\Delta p_0)H / \sigma$; $y \equiv z / H$. In 2D, there is only one scaling length − H as far as only one length variable z figures in the balance Eq. (12). The two constants of Eq. (13) A and C are determined by the boundary conditions at the lower/upper plate:

$$\cos \varphi_- = -\cos \theta_- = A \text{ at } y = 0 \text{ and } \cos \varphi_+ = \cos \theta_+ = Bo - C + A \text{ at } y = 1, \tag{14}$$

The signs of $\cos \varphi_\pm$ depend on the orientation of the normal vector towards the axis of symmetry, Figure 7.

The system of Eq. (13), (14) is still not the complete solution of the problem (12) but it contains abundant information about the characteristic 2D bridge profile points. For example the extremum points (waist/haunch) for which accounting that the current angle φ equals to 90°, from Eqs. (13) and (14) one obtains a quadratic equation with roots,

$$2y_e = 1 - \frac{\cos \theta_+ + \cos \theta_-}{Bo} \pm \sqrt{\left(\frac{\cos \theta_+ + \cos \theta_-}{Bo}\right)^2 - 2\frac{\cos \theta_+ - \cos \theta_-}{Bo} + 1}, \tag{15}$$

From Eq. (15) one can reveal many details connected with 2D bridge profile but before that it must be defined the area of $\theta_{\pm}$ and Bo values inside which a $2D$ bridge exists. The solution of this problem follows from the consideration that $|\cos\varphi| \leq 1$, i.e. $|Bo\,y^2 - Cy + A| \leq 1$. As far the left-hand side is a function of y, the inequality concerns its extremum point, i.e. $|-C^2/4Bo + A| \leq 1$ and after substituting the already determined constant A from (14) one obtains,

$$Bo \leq 2(1 + \cos\theta_-)[1 + \frac{\cos\theta_+ + \cos\theta_-}{1 + \cos\theta_-} + \sqrt{1 + 2\frac{\cos\theta_+ + \cos\theta_-}{1 + \cos\theta_-}}], \tag{16}$$

From Eq. (16) it follows that CBs with $\theta_- < \theta_+$ allow higher Bo values in comparison with $\theta_- > \theta_+$. For instance, at $\theta_+ = 180°$; $\theta_- = 0°$, $Bo \leq 8$, while in the reverse case, $\theta_+ = 0$; $\theta_- = 180°$, $Bo = 0$. Moreover, at $\theta_- = 180°$ any heavy bridge cannot exist.
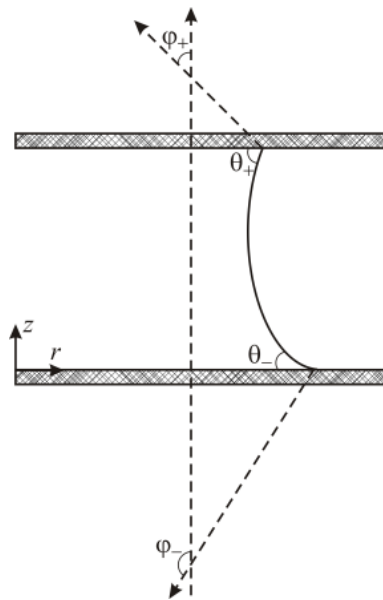

Figure 7. Sketch illustrating the *relations between the angles $\theta_{\pm}$ and $\varphi_{\pm}$*

Other indicative points are the TPC co-ordinates $X_{\pm}$, where $X_- = x(y=0)$, $X_+ = x(y=1)$. These co-ordinates are related with the parameters, $\theta_{\pm}$ and Bo via the integral of Eq. (13), whose concise form reads,

$$\Delta X = -\int_0^1 \cot\varphi\,dy, \tag{17}$$

It should be noted that here only the difference $X_+ - X_- = \Delta X$ is reasonable, because of the translation invariance of 2D problem.

According to Eqs. (13), (14), and (17), ΔX depends on three parameters $\Delta X\,(\theta_{\pm}, Bo)$. As mentioned many times, the value and behavior of $\theta_{\pm}$ depend on the particular TPC rheology. So for instance, without hysteresis $\theta_{\pm} = const$, while in the general case (in presence of hysteresis)

they are function of Bo, $\theta_\pm(Bo)$. Figure 8 represents experimental data of a typical contact angles dependence on bridge thickness H. With stretching the two contact angles show increasing difference, more accurate the upper angle θ_+ changes while the lower angle θ_- remains practically constant.
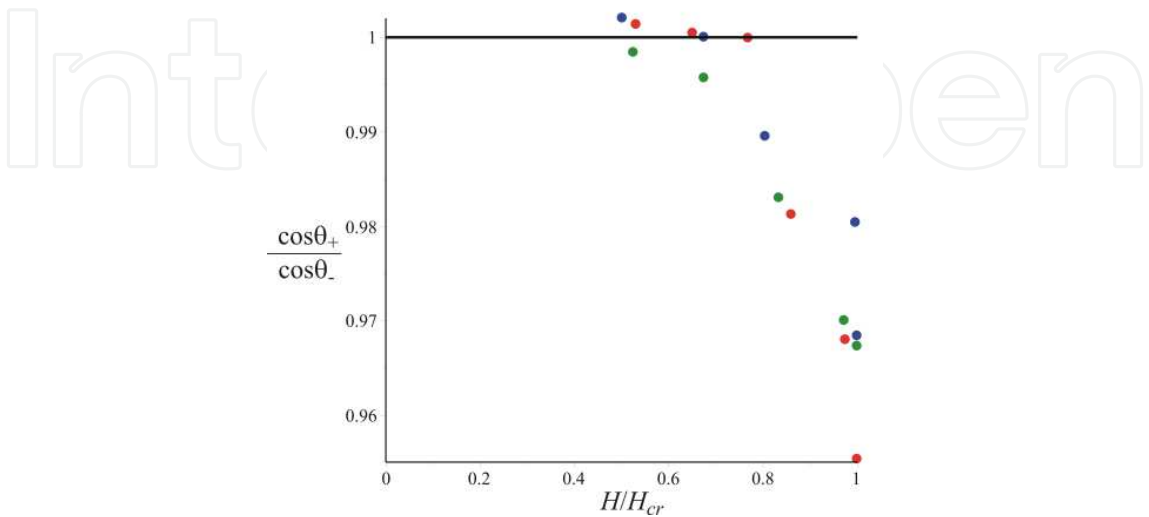

Figure 8. *Experimental results illustrating the ratio of the upper/lower contact angle $\theta_\pm$ as a function of the thickness ratio H/H_{cr} of IL concave CBs; green– IL_4; blue – IL_5; red–IL_6;*

Figure 9 presents theoretical curves (isogons) calculated on the basis of Eq. (17) compared with experimental data. The isogons are calculated at constant parameter $\theta_- = 0$ (complete wetting) and increasing θ_+ from 0° to 45° with step of 5°. Note that due to the relation $Bo \sim H^2$, the isogons actually describe the dependence $\Delta X(H)$. The θ -values are chosen to be close to the experimental ones.
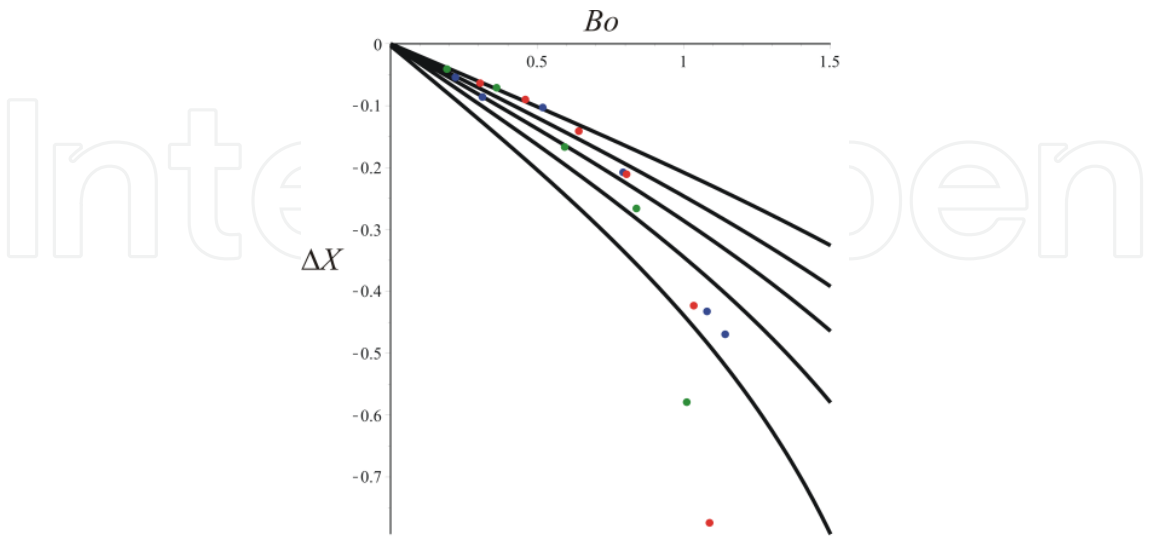

Figure 9. *Theoretical curves (isogones) ΔX vs. Bond number, calculated by Eq. (17). The points represent experimental data from concave CBs (hydrophilic plates): green – IL_4; blue – IL_5; red –IL_6.*

5. Experimental section

There are number of experimental methodologies concerning capillary bridges. Most of them are developed in order to utilize CBs as convenient tool for TPC properties, adhesive and capillary forces investigation. Over the past decade, there are some data in the literature which covers mainly the force aspect of capillary bridges. Most authors as Wei et al. [56], Yang et al. [57], Bradley et al., [58] etc. prefer to form capillary bridge at the tip of an AFM where they can measure the force directly. Others like Lee et al. [59] and Lipowsky et al. [60] offer various setups, which focus on directly capturing the CB profile. In this section, we will present similar setup with original image and statistical analysis

5.1. Experimental setup

Our experimental setup consists of a micrometer, onto the measuring arms of which two square (20x20x2 mm) stainless steel supporting plates were fixed, parallel to one another.

Two 22x22 mm microscope cover glasses (ISOLAB) of soda lime silica composition were selected as working surfaces. They were glued to the supporting plates for static measurements. Images were recorded by using a high speed camera, MotionXtra N3, which was mounted onto a horizontal optical tube with appropriate magnification, Figure 10.
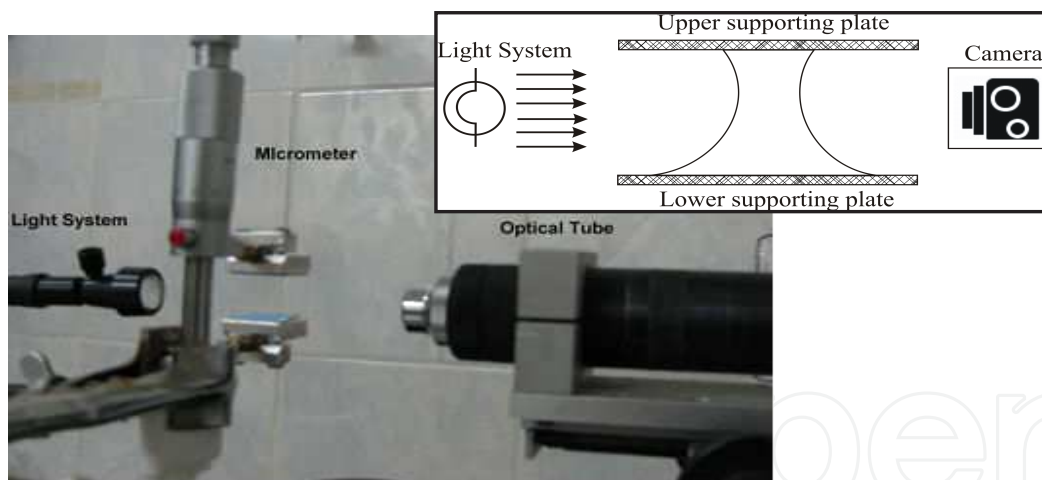

Figure 10. A picture and a schematic representation of the experimental setup

The light system was designed for the bundle of light to be directed perpendicularly to the electronic sensor of a high speed camera and at the same time the waist of the photographed CB to appear exactly at the middle position in the light bundle.

5.2. Solid surface preparation

Hydrophilic glass surfaces were pre-cleaned with 99.9% C_2H_5OH and washed with deionized (Millipore) water before being glued to the supporting plates.

All experiments were carried out with deionized (Milipore) water or ionic liquids (IL).

Hydrophobized glass cover slides have been used for the convex CB. The preliminary hydrophobization was done with PDMS (Rhodia Silicones, 47V1000), following the procedure described in [61]. Before gluing the slides, they were washed with 99.9% C_2H_5OH.

The experimental protocol is the same for all surfaces and samples.

5.3. Water capillary bridges

A small droplet of $\approx 1\ mm^3$ volume was placed in the middle of the lower glass slide. The upper glass slide was moved toward the droplet until a capillary bridge was formed. Further, several equilibrium states were recorded; pressing the shape until thin film was formed. Afterwards stretching took place until breakage occurred (some selected sequential pictures of the experimental part are presented in Figure 3, Figure 4, and Figure 6. The experiment was repeated several times with varying initial droplet volume. Concerning the effects due to evaporation, the direct volume decrease played no role, since the theoretical relations are in scaled (volume invariant) form (Section 2, Eq. (8)). Other effects related to the evaporation (e.g. thermo-effects) were not observed.

6. Ionic liquid capillary bridges

Room-temperature ionic liquids (RTIL) show very promising properties in studies of liquid CBs. They are salts in liquid states and usually exhibit very low vapor pressure (10^{-10} Pa at 25°C), i.e. no volume changes occurred during the experiment. Three RTIL were used for CB formation between hydrophilic glass surfaces. Summary of their physical properties is presented in Table 1 and their ion structural formulae are given in Figure 11 [62].

Sample number	Ionic Liquid		Surface Tension, σ [mN/m]	Density, ϱ [kg/m³]	ϱ/σ, [s²/m³]
	Cation	Anion			
IL 4	EMIM	BTA	33.6	1548	0.046
IL 5	DiEMIM	BTA	31.6	1450	0.046
IL 6	Et$_3$Pic	BTA	32.9	1513	0.046

Table 1. Physical properties of IL

From the presented data in Table 1, it is seen that ratio ϱ/σ determining the Bond number, Eqs. (2) remains constant for all RTILs.
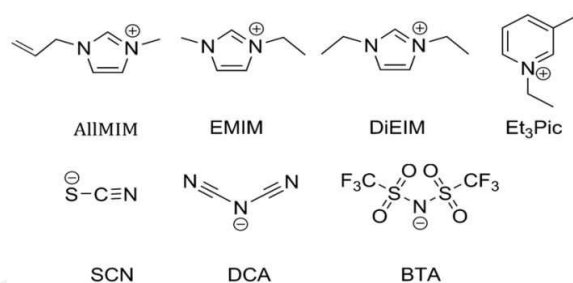
Figure 11. Structural formulae of ionic liquid ions

6.1. Image analysis

The image analysis consist of three essential steps: capturing the CB image, detection of CB profile edge and statistical approximation of the determined profile [63]. Below we've presented schematically each step with short comments.
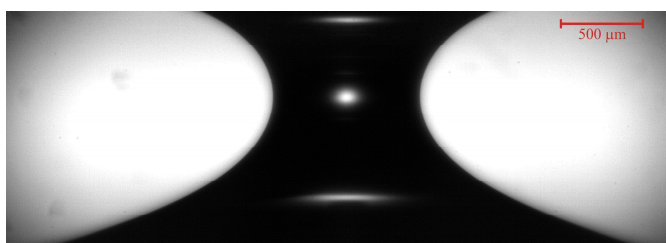
Capturing the CB image

Figure 12. *A typical CB image.* It's important to stress out that although the TPC region looks sharp, the contrast there isn't good enough. That's one of the reasons we choose to restrict us on the waist region.

6.1.1. Determining the CB profile

Determining the precise CB profile is the most vital part of the whole image analysis. This is why we pay special attention to it. It is performed in two steps: first we perform a rough edge detection (filtering the image) to get rid of the unnecessary information (background, light effects, etc.) and then scanning the filtered image to determine the precise profile.

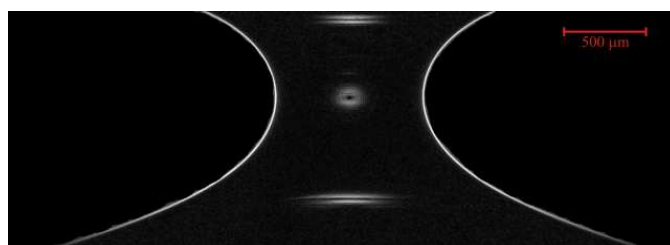• Finding edges with Sobel operator based filter [64].

Figure 13. Resulting image after applying the Sobel Filter on the image from Figure 12.

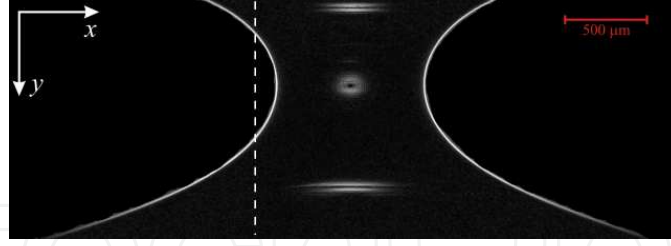- Scanning the filtered image (normal to the obtained contours)

Figure 14. For each point, y_i over a vertical stripe of the filtered picture (the white dashed line), the intensity value I_i is mapped, Figure 15.

- Determining the dynamic threshold

The average intensity of the signal $\bar{I}$ can be determined on every stripe of the image (Figure 15). Assuming that the obtained useful information is a small part of the entire signal, one can use the so-called "three-sigma rule" (webpage [65]) which is a measure for the noise exclusion. In the current case we use $3\sqrt{D}$ for the coefficient k, which multiplies the standard deviation.

$$t = \bar{I} \pm k\sqrt{D} \qquad \bar{I} = \frac{\sum_{Stripe} I_i}{n} \qquad D = \frac{\sum_{Stripe}\left(I_i - \bar{I}\right)^2}{n-1}$$

Here t is the calculated dynamic threshold; I_i is the intensity of the i–th point; $\bar{I}$ is the average intensity over a given stripe; k is a coefficient which controls the selection filter quality; D is the mean square deviation of the intensities; n is the number of y_i points.
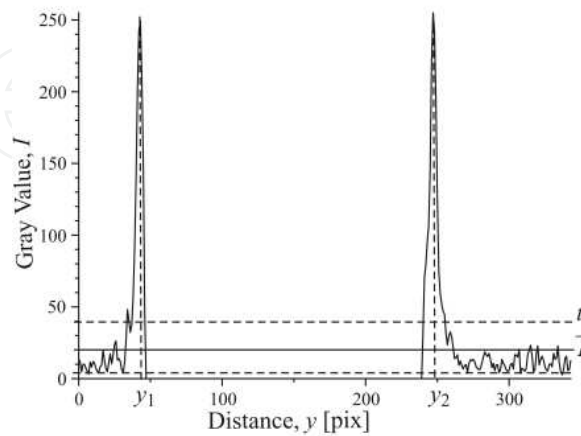

Figure 15. Pixel intensity over a stripe of the image. The exact positions y_i see below.

Averaging is done by a standard numerical approximation

$$y_i = \frac{\sum\limits_{I_j > t} I_j y_j}{\sum\limits_{I_j > t} I_j}$$

Here y_j is the coordinate of the i-th point and y_i is the averaged pixel coordinate (Figure 15). For all obtained points, x coordinates is with 1px precision (based on the scanning frequency), while y coordinates have sub-pixel precision compensating the Cartesian sampling of the sensor (Figure 16).
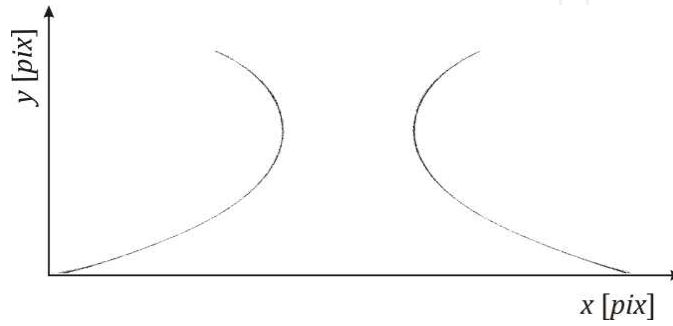

Figure 16. Resultant curve of established co-ordinates of the points in x,y [pixel] space.

6.1.2. Processing the obtained coordinates

- A selected segment of the meniscus profile with defined size (e.g. 150 points) is used.

- The points are submitted to a circular approximation:

$$\left(\frac{1}{K}\right)^2 = (x - x_0)^2 + (y - y_0)^2$$

- The calculation is repeated for successive sub-segments of points. Each approximation step delivers a radius of curvature, K^{-1}.

- From the obtained number of radii, the minimal value (the maximum curvature) is selected. We claim that it corresponds to the waist curvature. The precision of the procedure depends on the resolution of the respective profile which in this case is about 0.5μm.

This simple procedure gives us the opportunity to evaluate the curvature K^{-1} directly from the real CB profile and thus to make the validation of $2D \rightarrow 3D$ transition possible (Figure 6).

7. Summary

Presented are results of study of two types of CB systems. The first one covered investigations of CB in the absence of gravity. This is a demonstration of a geometrical approach combined

with the analytical description of the system, showing very good correlation with the experimental data. The second aspect is dedicated to CB behavior in gravity field. Here again the benefit of the combination of geometric and analytical methods is employed. The transparency of the obtained results holds out hope, the same approach to be successfully applied to other CB problems, e.g. CB stability.

Appendix A

In contrast to the variety of CB parameters near the critical height, their flattening (thinning) toward zero thickness, is of much more universal character. This universality starts to show itself at a thickness H, smaller than the radius of the contact R ($R \gg H$). Taking into account the self-evident fact that $R \to r_m \to \infty$ and $X (\equiv R / r_m) \to 1$ at $H \to 0$ makes suitable the substitution $X = 1 + \Delta$, with $\Delta \to 0$. Thus, the parameter C in the thin CB region tends to (Eq. (5)):

$$C(X = 1 - \Delta) \approx -\frac{1 - \sin \theta}{2\Delta} + \frac{1 + \sin \theta}{4} \tag{18}$$

The two terms on the right-hand side represent the two (dimensionless) curvatures: the meridional curvature (first term) and the azimuthal curvature (second term). For example, at $\theta = 90°$ we obtain a cylinder; the generatrix turns into a straight line of zero curvature, which leaves only the second (azimuthal) curvature equal to 1/2 and $C = 1/2$. The meridional curvature's change of sign as a function of the contact angle is allowed for by the sign of Δ.

It is worth commenting on the fact that the thin CB generatrices converge to equations of circle. It follows by inserting Eq. (18) in Eq. (4), which after integration yields,

$$y^2 + (x - 1 + X_c)^2 = X_c{}^2 \tag{19}$$

Note that within the framework of the thin CB approximation, the correct range of integration is $1 \le x \le 1 + \Delta$. The dimensionless circular radius $X_c = 1/2C$ (coinciding with the CB generatrix radii of curvature) is related to the CB thickness, via $H / 2r_m = X_c |\cos\theta|$. The use of modulus sign is meant to eliminate the sign alteration when the angle θ passes through $\pi/2$ (see above). The capillary pressure, C is represented by the first term on the right-hand side of Eq. (18), $X_c = 1/2C$. Equation (19) can be generalized as:

$$y^2 + (x - 1 \pm X_c)^2 = X_c^2 \tag{20}$$

Where, the positive sign is for $\theta < \pi/2$ and negative for $\theta > \pi/2$.

Estimation of the external force F acting upon thin CB can be obtained from Eq. (7) at $\Delta \to 0$ as follows:

$$F(X = 1 + \Delta) \approx \pi \gamma R (1 + \frac{1 - \sin \theta}{\Delta}) = \pi \gamma R \left(1 + 2R \frac{\cos \theta}{H} \right) \qquad (21)$$

By analogy to the capillary pressure, again for the case of $\theta \neq 90°$, the second term in the right-hand side is of interest, which eventually (upon sufficient thinning) becomes dominant $F(H \to 0) = 2\pi \gamma R^2 \cos \theta / H$. Allowing for the volume constancy ($\pi R^2 H = const$), makes the force F in the asymptotic dependence inversely proportional to the thickness of a square: $F(H \to 0) \sim 1 / H^2$. In the estimate of the volume, we have assumed that it equals to its cylindrical part, disregarding the menisci – an entirely correct approximation in case of sufficiently thin bridges.

Appendix B

A brief derivation and a mathematical analysis of the supporting forces ($F_\pm$) follows. Because of the double-meaning of the $z(r)$ curve, the integration is carried out separately for the two parts of CB volume (above and below the point r_m, Figure 1). And so, for the two parts we obtain:

$$\sigma 2\pi (r_m - R_- \sin \theta_-) = \pi (r_m^2 - R_-^2) \Delta p_0 - \rho g \pi \int_{R_-}^{r_m} z_- dr^2 \quad - \quad \text{for the lower part}$$

$$\sigma 2\pi (R_+ \sin \theta_+ - r_m) = \pi (R_+^2 - r_m^2) \Delta p_0 - \rho g \pi \int_{r_m}^{R_+} z_+ dr^2 \quad - \quad \text{for the upper part,} \qquad (22)$$

To clarify the matter, we present the integrals in (22) as follows:

$$\int_{R_-}^{r_m} z_- dr^2 = r_m^2 h_- - \int_0^{h_-} r^2 dz \to r_m^2 h_- - V_- / \pi;$$

$$\int_{r_m}^{R_+} z_+ dr^2 = R_+^2 H - r_m^2 h_- - \int_{h_-}^{H} r^2 dz \to R_+^2 H - r_m^2 h_- - V_+ / \pi, \qquad (23)$$

and when substitute (23) in (22), one obtains:

$$\sigma 2\pi(r_m - R_- \sin\theta_-) = \pi(r_m^2 - R_-^2)\Delta p_0 - \rho g\pi h_- r_m^2 + G_-$$
$$\sigma 2\pi(R_+ \sin\theta_+ - r_m) = \pi(R_+^2 - r_m^2)\Delta p_0 - \rho g\pi(R_+^2 H - r_m^2 h_-) + G_+, \tag{24}$$

where $G_\pm = \varrho g V_\pm$ is the respected weights of the upper/lower CB parts; $V_\pm$ – their volume parts. Actually Eqs. (24) define the pressure difference Δp_0

$$\Delta p_0 = -\frac{2\sigma(r_m - R_- \sin\theta_-) + \rho g h_- r_m^2 - G_-/\pi}{(R_-^2 - r_m^2)} =$$
$$= \frac{2\sigma(R_+ \sin\theta_+ - r_m) + \rho g(HR_+^2 - h_- r_m^2) - G_+/\pi}{(R_+^2 - r_m^2)}, \tag{25}$$

As discussed in Section 3, resultant forces $F_\pm$ at CB plates can be expressed as follows,

$$\pm F_\pm = (p_\pm - p_e)\pi R_\pm^2 - 2\pi\sigma R_\pm \sin\theta_\pm, \tag{26}$$

where $p_\pm$ are the internal pressures on the upper/lower plate, i.e. $p_- = p_0$; $p_+ = p_0 - \rho g H$. Making use of the notations introduced in Section 2, the above equation can be rewritten as (compare with Eq.(6)),

$$F_+ = \pi R_+^2(\Delta p_0 - \rho g H) - 2\pi\sigma R_+ \sin\theta_+,$$
$$-F_- = \pi R_-^2 \Delta p_0 - 2\pi\sigma R_- \sin\theta_-, \tag{27}$$

After substituting Δp_0 from (25) in (27), we come to the final expression for the force

$$a) F_+ = 2\pi\sigma R_+ \sin\theta_+ - \pi R_+^2(\Delta P - \rho g H) =$$
$$= \pi R_+ \frac{2\sigma r_m(R_+ - r_m \sin\theta_+) + R_+(G_+/\pi - \rho g r_m^2 h_+)}{R_+^2 - r_m^2};$$

$$b) F_- = \pi R_-^2 \Delta P - 2\pi\sigma R_- \sin\theta_- =$$
$$= -\pi R_- \frac{2\sigma r_m(R_- - r_m \sin\theta_-) - R_-(G_-/\pi - \rho g r_m^2 h_-)}{R_-^2 - r_m^2}. \tag{28}$$

As at any mechanical equilibrium the following ballance is valid $F_+ + F_- + G = 0$

Appendix C

References	Topics
H.M. Budgett, Proc. R. Soc. London A, 86 (1912) 25 W. Stone, Phil. Mag. 9 (1930) 610 J.S. McFarlane, D. Tabor, Proc. R. Soc. London A, 202 (1950) 224 R.E. Johnson Jr., R.H.J. Dettre, Phys. Chem. 68, 1744 (1964) L.W. Schwartz, S. Garoff, Langmuir 1, 219 (1985) A. Lafuma, D. Quere, Nat. Mater. 2, 457 (2003) J.H. Snoeijer, B. Andreotti, Phys. Fluids 20, 057101 (2008) H. Yang, P. Jiang, Langmuir 26, 12598 (2010) J.W. Krumpfer, T.J. McCarthy, Faraday Discuss. 146, 103 (2010)	Adhesion of spherical drop to a flat plate, lotus effect, contact angle hysteresis
J.S. McFarlane, D. Tabor, Proc. R. Soc. London A, 202 (1950) 224 N.L. Cross, R.G. Picknett, Particle Adhesion in the Presence of a Liquid Film, in: H.R Johnson, D.H. Litter (Ed.), The Mechanism of Corrosion by Fuel Impurities, Butterworths, London, 1963; p. 383 G. Mason, W.C. Clark, Chem. Eng. Sci., 20 (1965) 859 W.C. Clark, J.M. Haynes, G. Mason, Chem. Eng. Sci., 23 (1968) 810 M.A. Erle, D.C. Dyson, N.R. Morrow, AIChE J., 17 (1971) 115	Capillary bridges between two solid spheres
A. Marmur, Langmuir, 9 (1993) 1922 R.A. Fisher, J. Agric. Sci., 16 (1926) 492 W. Rose, J. Appl. Phys., 29 (1958) 687 N.L. Cross, R.G. Picknett, Trans. Faraday Soc., 59 (1963) 846 J.C. Melrose, AIChE J., 12 (1966) 986 W.C. Clark, J.M. Haynes, G. Mason, Chem. Eng. Sci., 23 (1968) 810 M.A. Erle, D.C. Dyson, N.R. Morrow, AIChE J., 17 (1971) 115 F.M. Orr, L.E. Scriven, A.P. Rivas, J. Fluid Mech., 67 (1975) 723 Brakke, K. Exp. Math,1992, 1 (2), 141-65 Concus, P. and R. Finn. SIAM J Math. Anal., 27(1)(1996), 56-69 A. C. King, J. R. Ockendon, H. Ockendon, Q. J. Mech. Appl. Math., 52(1) (1999), 73-9	Exact solution of Laplace equation of capillarity between two solids
G.I. Taylor, D.H. Michael, J. Fluid Mech., 58 (1973) 625 M.L. Forcada, M.M. Jakas, A. Gras-Marti, J. Chem. Phys., 95 (1991) 706 G. Debregeas, F. Brochard-Wyart, J. Colloid Interface Sci., 190 (1997) 134 F. Restagno, C. Poulard, C. Cohen, L. Vagharchakian, L. Leger, Langmuir 25, 11188 (2009) L. Vagharchakian, F. Restagno, L. Leger, J. Phys. Chem. B 113, 3769 (2009)	Capillary bridges between *solid* and *fluid* phases
W.A. Ducker, Z. Xu, J.N. Israelachvili, Langmuir, 10 (1994) 3279 M.L. Fielden, R.A. Hayes, J. Ralston, Langmuir, 12 (1996) 3721	Capillary-bridge-type meniscus
S. Ross, J. Phys. Colloid Chem., 54 (1950) 429 P.R. Garrett, J. Colloid Interface Sci., 76 (1980) 587	Capillary bridges between two fluid phases

References	Topics
P.R. Garrett, in: P.R. Garrett (Ed.), Defoaming: Theory and Industrial Applications, M. Dekker, New York, 1993; Chapter 1	
R. Aveyard, P. Cooper, P.D.I. Fletcher, C.E. Rutherford, Langmuir, 9 (1993) 604	
R. Aveyard, B.P. Binks, P.D.I. Fletcher, T.G. Peck, C.E. Rutherford, Adv. ColloidInterface Sci., 48 (1994) 93	
R. Aveyard, J.H. Clint, J. Chem. Soc. Faraday Trans., 93 (1997) 1397	
N.D. Denkov, P. Cooper, J.-Y. Martin, Langmuir, 15 (1999) 8514	
N.D. Denkov, Langmuir, 15 (1999) 8530	

Glossary

Bo – bond number

CB – capillary bridge

C – dimensionless capillary pressure

$F_{\pm}$ – external forces

G – CB weight

H – bridge thickness

K – curvature

L_r / L_z – radial/axial scaling length

R – equilibrium dimension radius

$R_{1,2}$ – meridional/azimuthal curvature radiuses

$R_{\pm}$ – upper/lower dimension radius

RTIL – Room-Temperature Ionic Liquid

TPC – Three-Phase Contact

X – dimensionless radius R/r_m

g – gravity of earth

$p_{i/e}$ – internal/external pressures

p_{σ} – capillary pressure

r_m – dimension waist radius

$x \equiv r / r_m; y \equiv z / H$ – current dimensionless coordinates

Δp – pressure difference

$\theta_\pm$ − upper/lower contact angle

$\varrho_{liquid|air}$ − liquid|air density

σ − surface tension

Acknowledgements

Author details

Boryan P. Radoev[1*], Plamen V. Petkov[2] and Ivan T. Ivanov[1]

*Address all correspondence to: fhbr@lchem.uni-sofia.bg

1 Sofia University "St. Kliment Ohridski", Faculty of Chemistry and Pharmacy, Department of Physical Chemistry, Sofia, Bulgaria

2 Sofia University "St. Kliment Ohridski", Faculty of Chemistry and Pharmacy, Department of Pharmaceutical and Chemical Engineering, Sofia, Bulgaria

References

[1] Fall A., Weber B., Pakpour M., Lenoir N., Shahidzadeh N., Fiscina J., Wagner C., and Bonn D. Sliding friction on wet and dry sand. Phys. Rev. Lett. 2014; 112 175502

[2] Dobrokhotov V., Yazdanapanah M., Hosseini M., Pabba S., Berry S. M., Safir A., Keynton R. S., and Cohn R. W. Liquid property measurements using constant diameter nanoneedletipped AFM probes. 6th Intl. Symp. on Contact Angle, Wettability and Adhesion. Orono, ME 2008

[3] Men Y., Zhang X. and Wang W. Capillary liquid bridges in atomic force microscopy (AFM): Formation, rupture, and hysteresis. J. Chem. Phys. 2009; 131 184702

[4] Avouris Ph., Hertel T., Martel R. Atomic force microscope tip-induced local oxidation of silicon: Kinetics, mechanism, and nanofabrication. Appl. Phys. Lett. 1997; 71(2) 285-287

[5] Landis S. Investigation of capillary bridges growth in NIL process, 23rd European Mask and Lithography Conference (EMLC) 2007

[6] Bandic Z., Dobisz E., Wu T., Albrecht T. Patterning on hard disk drives. Solid State Technol. 2006; 57-59

[7] Dagata J., Inoe T., Itoh J., Yokayama H. Undestanding scanned probe oxidation of silicon. Appl. Phys. Lett. 1998; 73(2) 271-273

[8] Acikgoza C., Hempeniusa M., Huskensb J., Vancso G. Polymers in conventional and alternative lithography for the fabrication of nanostructures. European Polymer Journal 2011; 47(11) 2033-2052

[9] Gabrieli1 F., Lambert P., Cola1 S., and Calvetti F. Micromechanical modelling of erosion due to evaporation in a partially wet granular slope. Int. J. Num. Anal. Methods in Geomechanics 2012; 36(7) 918-943

[10] Pepin X., Rossetti D., Iveson, and Simons S. Modeling the evolution and rupture of pendular liquid bridges in the presence of large wetting hysteresis. J. Col. Int. Sci. 2000; 232 289-297

[11] Lu N., Lechman J. and Miller K. Experimental verification of capillary force and water retention between uneven-sized spheres. J. Eng. Mech. 2008; 385

[12] Delaunay C. Sur la Surface de Revolution dont la Courbure Moyenne est Constante. J. Math. Pures Appl. 1841; 6 309-314

[13] Kenmotsu, K., Surfaces of revolution with prescribed mean curvature, Tohoku Math. J. 1980; 32 147-153.

[14] Euler L. Methodus inveniendi lineas curvas maximi minimive proprietate gaudentes. Opera omnia 1744; 24(1)

[15] Plateau J. Statique expérimentale et théorique des liquides soumis aux seules forces moléculaires. Gauthier-Villars 1873;

[16] Young, T. An essay on the cohesion of fluids. Philos. Trans. R.Soc. London 1805; 95 65-87.

[17] De Gennes P.G., and Prost J. The Physics of Liquid Crystals. Oxford: Clarendon Press 1993

[18] Princen N.M. The equilibrium shape of interfaces, drops and bubbles. in Matijievich E. Ed. Rigid and Deformable Particles at Interfaces, in Surface and Colloid Science. New York: Willey-Interscience 1969

[19] Hadjilazova M., Mladenov I., and Oprea J. Unduloids and their geometry. Archivium Mathematicum (BRNO) 2007; 43 417-429

[20] Myshkis A.D., and Babskii V.G. Low-Gravity Fluid Mechanics: Mathematical Theory of Capillary Phenomena. Springer-Verlag 1987

[21] Eral H. B. et al. Contact angle hysteresis: a review of fundamentals and applications. Colloid Polym. Sci 2013; 291(2) 247-260

[22] De Gennes P.G., Brochard-Wyart F., Quéré D., Widom B. Capillarity and wetting phenomena: drops, bubbles, pearls. Waves Phys. Today 2004; 57 66-67

[23] Fisher R.A. On the capillary forces in an ideal soil: correction of formulae given by W. B. Haines. The Journal of Agricultural Science 1926; 16(3) 492-505

[24] Batchelor G.K. An Introduction to Fluid Dynamics. Cambridge Univ. Press 1970

[25] Gao P., Lu X.Y. On the wetting dynamics in a Couette fow. J. Fluid Mech. 2013; 724 1-12

[26] Voinov, O. V. Hydrodynamics of wetting. Fluid Dyn. 1976;11 714-721

[27] Cox R.G. J. Fluid Mech. 1986; 168 169

[28] Cox R.G. J. Fluid Mech. 1986; 168 195

[29] Dussan E.B., Davis S.H. Motion of a fluid–fluid interface along a solid surface. J. Fluid Mech. 1974; 65 71-95

[30] Vinogradova O.I. Int. J. Miner. Process 1999; 56 31

[31] Eyring H. The Theory of Rate Processes: The Kinetics of I Chemical Reactions, Viscosity, Diffusion and Electrochemical Phenomena. New York: McGraw-Hill 1941

[32] Blake T.D., Haynes J.M. J. Col. Int. Sci. 1969; 30 421-423

[33] Churaev N.V., Derjaguin B.V., Muller V.M. Surface Forces. Springer Science and Business Media 1987

[34] Israelashvilly J. Intermolecular and Surface Forces, Third Edition: Revised. Elsevier 2011

[35] Starov V.M., Velarde M.G., Radke C. in J. Wetting and Spreading Dynamics. Surfactant Sci. Series, CRC Press 2007; 138

[36] Nicolis G., Prigogine I. Self-Organization in Non-equilibrium Systems. London: John Willey&Sons NY 1977

[37] Lord Rayleigh. On the instability of liquid jets. Proceedings of the mathematical society 1878; 10 4-13

[38] Nelson A. Rayleigh Instability of an Annulus 2000. http://willson.cm.utexas.edu/Research/Sub_Files/Surface_Phenomena/Spring%202000/Rayleigh_Instability_of_an_Annulus.pdf

[39] Deegan R.D., Bakajin O., Dupont T.F., Huber G., Nagel S.R., Witten T.A. Capillary flow as the cause of ring stains from dried liquid drops. Nature 1997; 389 827-829

[40] Deegan R.D., Bakajin O., Dupont T.F., Huber G., Nagel S.R., Witten T.A. Contact line deposits in an evaporating drop. Phys. Rev. E 2000; 62 756-765

[41] Girard F., Antoni M., Faure S., Steinchen A. Evaporation and Marangoni driven convection in small heated water droplets. Langmuir 2006; 22 11085-11091

[42] Kralchevsky P., Nagayama K. Particles at Fluid Interfaces and Membranes. Amsterdam: Elsevier 2001. p469-502

[43] Hager W.H. Wilfrid N. Bond and the Bond number. J. of Hydraulic Research 2012; 50(1) 3-9

[44] Perales J.M. et al. Adv. Space Res 1995; 16(7) 5-14

[45] Perales J.M. et al. European Journal of Mechanics B/Fluids 2003. 22(4) 355-368

[46] Ito M., Sato T. In situ observation of a soap-film catenoid: A simple educational physics experiment. European Journal of Physics 2010; 31(2) 357-365

[47] Petkov P.V., Radoev B.P. Statics and dynamics of capillary bridges. Col. and Surf. A Physicochemical and Engineering Aspects 2014; 460(20) 18-27

[48] Bashforth F., Adams J.C. An Attempt to Test the Theory of Capillary Attraction. London/New York: Cambridge Univ. Press 1883

[49] Adamson A.W. Physical Chemistry of Surfaces. New York: Interscience Publishers, Inc. N.Y 1960

[50] Huh C., Scriven L.E. J. Colloid Interface Sci. 1969; 30 323

[51] Padday J.F. The profiles of axially symmetric menisci. Phil. Trans. R. Soc. Lond. A. 1971; 269

[52] Padday J.F. Axisymmetric meniscus profiles. J. Coll. and Int. Sci. 1972; 38(2) 323-334

[53] Restagno et al. Langmuir 2009; 25(18) 11188-11196

[54] Danov K.D. et al. J. Col. and Int. Sci. 2015; 440 168-178

[55] Martinez I., Perales J. M. Acta Astronautica 1987; 15(8) 567-571,

[56] Wei et al., J. Phys. D: Appl. Phys 2007; 40 4368-4375

[57] Yang S.H.et al. Chemical Physics Letters 2008; 451 88-92

[58] Bradley R.H. et al. Phys. Chem. Chem. Phys. 2006; 8 2525-2530

[59] Lee, H.J. Langmuir 2013; 29 11028-11037

[60] Lipowsky R. Langmuir 2010; 26(24) 18734-18741

[61] Marinova K.G., Tcholakova S., Denkov N.D. Hydrophobization of glass surface by adsorption of polydimethylsiloxane (PDMS). Langmuir 2005; 21 11729-11737

[62] Ivanov I.T., Slavchov R.I et al. Wetting properties of low-viscosity room temperature imidazolium ionic liquids. Ann. Univ. Sofia, Fac. Chim. 2011; 102/103 259-271

[63] Abramoff M., Magalhaes P., Ram S. Image processing with image. J. Biophotonics International 2004; 11(7) 36-42

[64] Canny J.F. A computational approach to edge detection. IEEE Trans Pattern Analysis and Machine Intelligence 1986; 8(6) 679-698

[65] Nikulin M.S. Encyclopedia of Mathematics. URL: http://www.encyclopediaofmath.org/index.php?title=Three-sigma_rule&oldid=17366